

Large tunability of strain in WO₃ single-crystal microresonators controlled by exposure to H₂ gas

Nicola Manca^{†,1,2,3,*} Giordano Mattoni^{†,1,4} Marco Pelassa,⁵
Warner J. Venstra,^{1,6} Herre S. J. van der Zant,¹ and Andrea D. Caviglia¹

¹Kavli Institute of Nanoscience, Delft University of Technology, P.O. Box 5046, 2600 GA Delft, The Netherlands

²Dipartimento di Fisica, Università degli Studi di Genova, via Dodecaneso 33, Genova, Italy

³CNR-SPIN Institute for Superconductors, Innovative Materials and Devices, Corso Perrone 24, Genova, Italy[†]

⁴Department of Physics, Graduate School of Science, Kyoto University, Kyoto 606-8502, Japan

⁵Dipartimento Architettura e Design, Università degli Studi di Genova, Stradone S. Agostino 37, Genova, Italy

⁶Quantified Air BV, Rijnsburgersingel 77, 2316 XX Leiden, The Netherlands

This document is the Accepted Manuscript version of a Published Work that appeared in final form in ACS Applied Materials & Interfaces, copyright © American Chemical Society after peer review and technical editing by the publisher. To access the final edited and published work see <https://pubs.acs.org/doi/10.1021/acsami.9b14501>.

Strain engineering is one of the most effective approaches to manipulate the physical state of materials, control their electronic properties, and enable crucial functionalities. Because of their rich phase diagrams arising from competing ground states, quantum materials are an ideal playground for on-demand material control, and can be used to develop emergent technologies, such as adaptive electronics or neuromorphic computing. It was recently suggested that complex oxides could bring unprecedented functionalities to the field of nanomechanics, but the possibility of precisely controlling the stress state of materials is so far lacking. Here we demonstrate the wide and reversible manipulation of the stress state of single-crystal WO₃ by strain engineering controlled by catalytic hydrogenation. Progressive incorporation of hydrogen in freestanding ultra-thin structures determines large variations of their mechanical resonance frequencies and induces static deformation. Our results demonstrate hydrogen doping as a new paradigm to reversibly manipulate the mechanical properties of nanodevices based on materials control.

INTRODUCTION

Complex oxides are characterised by a rich energy landscape governed by multiple thermodynamic parameters, including temperature, stress, chemical potential, and electromagnetic fields.[1–3] Phase competition in these quantum materials leads to giant responses to external stimuli associated with large and non-linear susceptibilities. Chemical doping is a powerful control parameter to switch between their competing phases, and oxygen vacancies have often been employed to induce changes in electrical, structural or magnetic properties, although with limited reversibility.[4–7] Hydrogen intercalation is an alternative route to effectively control the ground state of these materials, as an example, by stabilizing metallic phases and promoting lattice symmetry,[8–10] but the possibility of precisely controlling the stress state is so far lacking. A particularly interesting system with multiple competing ground states regulated by anharmonic couplings between different structural distortions is WO₃.^[11] Its complex energy landscape determines large changes of its lattice and electronic properties in response to chemical doping,^[12] electric fields,^[13] and epitaxial strain.^[14] These characteristics have important technological applications, such

as electrochromic devices, smart windows,^[15–17] and gas sensing where record-holding pmm sensitivity to H₂ was recently demonstrated.^[18]

Here we show that the electromechanical response of freestanding single-crystal WO₃ microbridges can be reversibly controlled by hydrogen gas at room temperature. The incorporation of hydrogen in WO₃ thin films induces a change in the out-of-plane lattice constant up to 1.3%, an effect that we use to tune the mechanical resonances of WO₃ microbridges as their stress state changes from tensile to compressive.

RESULTS AND DISCUSSION

This experiment is performed on a 50 nm-thick single crystal WO₃ film grown on top of a Ti-terminated SrTiO₃ (001) substrate. The WO₃ thin film shows a flat surface with a step-and-terrace morphology that indicates good heteroepitaxial growth (film characterisation in Supporting Information, Sec. I). A small amount of Pt, of equivalent thickness 0.2 nm, is then deposited by e-beam evaporation to enable hydrogen intercalation, as described in the Methods section and in Ref. 18. We note that the hydrogen incorporation rate can be regulated by the amount of Pt catalyst: here we choose to use a low amount in order to slow down the process and monitor it as a function of time. The single-crystal character of WO₃ is confirmed by X-ray characterisation, where nar-

* manca@fisica.unige.it

[†] These two authors contributed equally

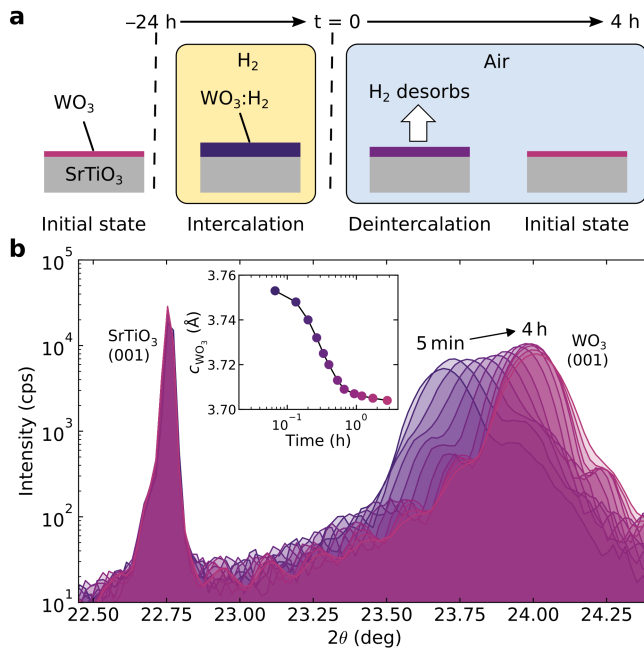


FIG. 1. **Lattice expansion due to hydrogen doping in WO₃ thin films.** (a) Schematic representation of the experiment showing hydrogen intercalation in a 20% H₂/Ar mixture and deintercalation in air. (b) X-ray scan showing the sharp (001) peak of the SrTiO₃ substrate and WO₃(001) peak with its finite size oscillations during hydrogen deintercalation. The inset shows the variation of WO₃ c -axis length as a function of time.

row rocking curves and reciprocal space maps show that the film is coherently strained to the substrate lattice. θ - 2θ scans along the (001) and (002) peaks of WO₃ present finite size oscillations, indicating high crystal quality (see Supporting Information, Sec. II). From the X-ray data we extract a c -axis length of 3.70 Å, in agreement with previous reports of WO₃ thin films on SrTiO₃.^[12] Considering that in its bulk pseudocubic phase WO₃ has a lattice constant of about 3.77 Å,^[19] epitaxial lock imposed by the substrate determines an elongation of the a and b axes of about 3.4%, with a consequent decrease of the c -axis that in our film amounts to -2% . The film is hence under in-plane tensile stress. This analysis indicates that the unit cell volume in thin films is slightly larger than in bulk. This is expected and could be related to two mechanisms: a Poisson's ratio lower than 0.5 and the presence of oxygen vacancies. While the former contribution is present in the vast majority of compounds, the presence of oxygen vacancies is almost unavoidable in WO₃ thin films with optimal structural quality,^[12] and most probably constitute one of the main relaxation mechanisms for epitaxial strain.

We measure the structural response of WO₃ to H₂ gas by monitoring changes in its c -axis parameter by X-ray diffraction. The experimental procedure comprises the two steps illustrated in Figure 1(a): The sample is initially placed at room temperature in a sealed chamber filled with 1 bar of a 20% H₂/Ar mixture for 24 h (inter-

calation) to achieve a stable (saturated) hydrogen doping condition. When transferred to the XRD setup, the sample is exposed to air at $t = 0$. In this step, hydrogen is released from the WO₃ lattice (deintercalation) and the material progressively regains its initial state. Fig. 1(b) shows several θ - 2θ scans taken during hydrogen deintercalation, where a progressive shift of the WO₃(001) peak and its finite size oscillations occurs. This shift corresponds to a change in WO₃ c -axis parameter which is reported as a function of time in Fig. 1(b). In the hydrogen-doped state at $t = 5$ min we measure $c_{WO_3} = 3.75$ Å, indicating an increase of about 1.25% with respect to the undoped condition. Upon hydrogen deintercalation, c_{WO_3} progressively decreases and recovers the value of the initial state after about 1 h. This indicates that hydrogen determines a large and reversible expansion of the WO₃ lattice, with a magnitude comparable to what has been previously reported upon the formation of oxygen vacancies or intercalation of alkali metals.^[12, 19, 20]

The large lattice expansion induced by hydrogen doping offers the interesting possibility to control the mechanical stress of the material in a reversible manner. To explore this possibility, we realize WO₃ freestanding microbridges. The structures are fabricated by using lithographic patterning and combined dry/wet etching processes in order to remove the SrTiO₃ substrate, a procedure similar to the one used in previous reports.^[4] (see also Methods section and Supporting Information, Sec. III). Figure 2(a) shows the false-colour micrograph of a typical WO₃ microbridge acquired by scanning electron microscopy. The freestanding structure (5 μ m-wide, 110 μ m-long) is composed of a 50 nm-thick WO₃ crystalline thin film (purple), and 50 nm-thick gold elements (yellow) comprising two 5 μ m \times 5 μ m mirrors and a 1 μ m-wide microwire that runs throughout the freestanding region. The mirrors are used to reflect the laser light employed to measure the mechanical motion of the bridge in an optical lever geometry (Fig. 2(b)), while the microwire provides a low-impedance electrical channel required for the electrical excitation. By applying an alternating electrical current through the gold wire, the microstructure is mechanically actuated via the magnetomotive and electrothermal mechanisms (see Methods). The typical mechanical spectra of a pristine 110 μ m-long microbridge is shown in Fig. 2(c). We also fabricated microbridges of other lengths between 50 and 110 μ m, all of which show similar spectra (see Supporting Information, Sec. IV). The fundamental resonance mode of the longer beams shows a better signal-to-noise ratio compared to the shorter ones, as expected due to a larger deflection. Furthermore, a higher quality factor is observed, which is attributed to lower clamping losses (see Supporting Information, Sec. V). For this reason, we focus on the 110 μ m-long microbridge to investigate the changes induced by hydrogen incorporation.

The simultaneous mechanical and electrical characterization is performed in a vacuum chamber with variable

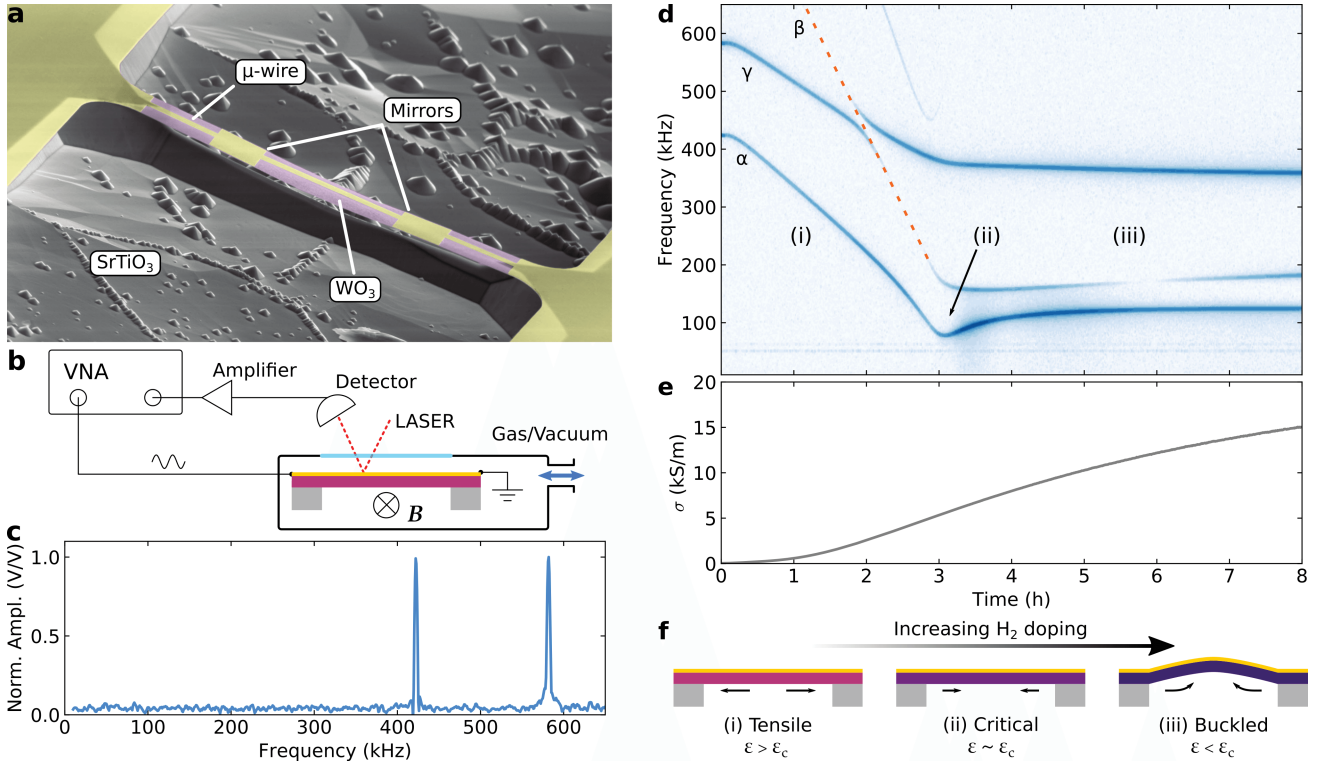


FIG. 2. **Hydrogen doping of single-crystal WO_3 microbridges.** (a) Scanning electron micrograph in false colors of the measured device. (b) Schematic of the experimental setup (VNA, vector network analyser). (c) Mechanical spectrum of a $110\ \mu\text{m}$ -long microbridge in the pristine state. (d) Colormap of the mechanical spectra of the microbridge in (a) as a function of time when exposed to 5 mbar of 20% H_2/Ar gas mixture and (e) electrical conductivity measured at the same time. (f) Illustration of the three regimes identified in (d). The color-scale in (d) is linear and normalized in V/V .

gas environment, optical access, and a controlled sample temperature fixed at 25°C . The WO_3 device is initially in an undoped condition and we measure its mechanical spectrum as a function of time in Figure 2(d). Details of the optical setup employed in this experiment are reported in the Supporting Information, Sec VI. At $t = 0$ we introduce a 20% H_2/Ar mixture at low pressure (0.5 mbar) to follow the hydrogen intercalation dynamics with minimal damping of the mechanical motion. Hydrogen doping results in a dramatic change in the mechanical behaviour of the microbridge which can be divided into three distinct regions: (i) a steep decrease of the eigenfrequencies, (ii) a transitional regime, and (iii) a flat response. The lowest mechanical mode α has a smooth behaviour across the different regions and corresponds to the first flexural mode, as discussed in the following. At $t = 0$ the WO_3 microbridge is in a tensile strain state originating from the lattice mismatch with the SrTiO_3 substrate. In this condition, the structure can be schematically modelled as an ideal thin and long double-clamped beam where the flexural resonance frequencies are given by the Euler-Bernoulli equation[21]

$$f_n(\varepsilon) = a_n \frac{t}{l^2} \sqrt{\frac{E}{\rho} \left(\frac{1}{(1-\nu^2)} + b_n \varepsilon \left(\frac{l}{t} \right)^2 \right)}, \quad (1)$$

with resonance frequency f_n relative to the n^{th} mode, axial strain ε , Young modulus E , density ρ , Poisson ratio ν , length l , and thickness t . a_n and b_n are numerical coefficients related to the mode shape. Eq. (1) shows that the mechanical eigenfrequencies of the microbridge change as a function of strain ε . In our experiment ε changes continuously over time due to the large WO_3 lattice expansion during hydrogen intercalation (Fig. 1). The most dramatic effect is observed in region (i), where the relaxation of the initial tensile strain results in a large drop of the resonance frequencies. According to Eq. (1) the frequency of the first flexural mode $f_1(\varepsilon)$ is expected to reach zero at the critical strain value

$$\varepsilon_c = -\frac{1}{1-\nu^2} \left(\frac{t}{l} \right)^2 \frac{1}{b_1}. \quad (2)$$

However, in real systems this is typically not observed because device asymmetry causes the frequency to reach a smooth minimum at the finite strain value ε_c . [22] In our experiment this occurs in region (ii) at $t \sim 3\text{ h}$, where the resonance frequency of the lowest mode α shows a minimum at $f = 80\text{ Hz}$, about one fifth of its initial value. A further increase of the compressive strain causes out-of-plane buckling. This occurs in region (iii), where Eq. 1 is not applicable and the resonance frequency of α increases again as the excess compressive strain energy is stored in the form of out-of-plane de-

formation (buckling). At the onset of the buckled state, the frequencies of the odd mechanical modes are expected to rise slightly,[22–24] consistent with the small frequency increase that α undergoes in region (ii). Multiple higher-order modes are visible in the spectral map of Fig. 2(d), with frequencies above α . Their frequencies cannot be represented by a simple string resonator because interfacial stress and non-uniform mass distribution play an important role. These resonances are probably related to torsional and flexural modes of even order which show different response to strain,[23] as discussed in the last part of this work. An avoided crossing between modes β and γ occurs at around $t = 2$ h, indicating a strong coupling between the mechanical modes. This feature arises as each mode shows a different tuning slope with applied compressive stress.[23–25] Finally, we note that the data reported in Fig. 2(d) are in good qualitative agreement with similar measurements performed during hydrogen deintercalation in air, thus showing good reversibility of the process (Supporting Information, Sec. VII).

During hydrogen intercalation we also measure the time dependence of the electrical conductivity of WO_3 (σ_{WO_3}), which is reported in Fig. 2(e). In our device design, the conductivity of the microbridge is always determined by the gold microwire, whose constant electrical resistance (50Ω) is much lower than that of WO_3 at any level of hydrogen doping. For this reason, we monitor σ_{WO_3} on a separate region of the film close to the microbridge. The data shows the progressive metallization of the material due to electronic doping, in agreement with previous reports.[18] Hydrogen intercalation progresses smoothly during the whole experiment and saturation occurs only towards the end of the measured time span ($t > 8$ h). This indicates that between $t = 4$ and 8 h the amount of hydrogen in the WO_3 lattice is significantly increasing, even if the mechanical modes show a flat response. We note that, albeit the suspended WO_3 microbridge has a higher surface area exposed to H_2 gas compared to the clamped film, in both cases the Pt catalyst is present only on the top surface, thus determining the same rate of hydrogen intercalation. Furthermore, the rate of hydrogen dynamics in this experiment is significantly longer than during the XRD measurements of Fig. 1 because of the low hydrogen pressure, and the different rates of intercalation and deintercalation.[18] The observed evolution of the microbridge mechanical states is schematically summarised in Fig. 2(f).

A strong evidence of the insurgence of a buckled state upon the intercalation of hydrogen can be obtained by optical microscopy. For this purpose, we report in Figure 3 a series of photographs showing one gold mirror of the microbridge. For this experiment the microbridge is first prepared in a saturated-doping state and at $t = 0$ it is exposed to air at room temperature, the same procedure used in Fig. 1. The photographs are acquired at different times with an objective lens (depth of field of

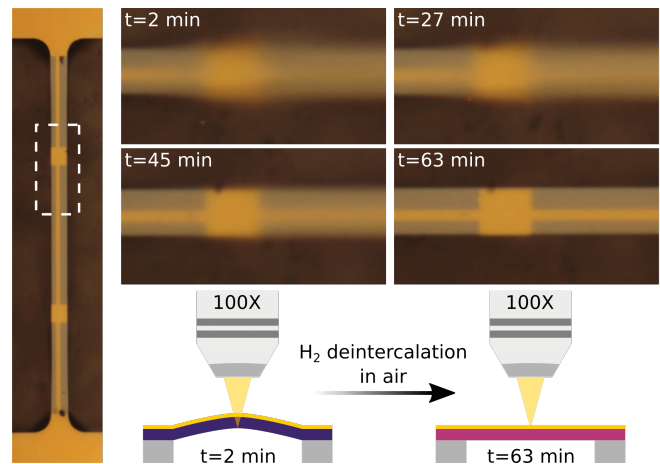


FIG. 3. Relaxation of the buckled state upon hydrogen deintercalation. Optical images of the WO_3 microbridge of Fig. 2(a) initially in a condition of saturated doping and exposed to air at $t = 0$. The white dashed rectangle indicates the magnified region. The schematic drawing illustrates how relaxation of the buckled state brings back the microbridge in the microscope focal plane.

about $0.7 \mu\text{m}$) whose focal plane is fixed to have in focus the clamped edges of the microbridge. In the initial state at $t = 2$ min the mirror is out of focus, indicating static deformation in the direction perpendicular to the focal plane. The structure gradually gets more in focus at $t = 45$ min, and at $t = 63$ min, after about one hour in air, the whole microbridge is in focus, indicating the recovery of a flat state in the undoped conditions. We note that this time span of hydrogen deintercalation in 1 bar of air is comparable to the one of the XRD measurements of Fig. 1 and, as previously discussed, much faster than the slow dynamics observed in Fig. 2.

To better understand the changes of the WO_3 microbridge mechanical properties, we perform a finite element analysis as a function of strain (details in Methods and Supporting Information, Sec. VIII). The strain-dependence of the three lowest modes of the simulated device and the corresponding mode shapes are reported in Figures 4(a) and 4(b), respectively. The trend of the frequencies well represents our experimental data, with a rapid decrease of the first and second flexural modes α , β , and a slower variation of the torsional mode γ . Due to their different slope, β and γ intersect at about $f = 1.3$ MHz (intersection of mode α with the grey dotted line). Also the presence of a mode crossing is consistent with our experimental results, where it occurs around $f = 0.45$ MHz (Fig. 2(d)). We note that the experimental crossing frequency is about three times smaller than the simulated one, a discrepancy probably caused by the fact that we used values of E_{WO_3} and ν_{WO_3} from first principles since no experimental data is available in literature.[26] However, the strain value corresponding to the crossing point in our simulations is weakly dependent on E and ν (Supporting Information, Sec VIII), and can thus be used as a reference to estimate the in-

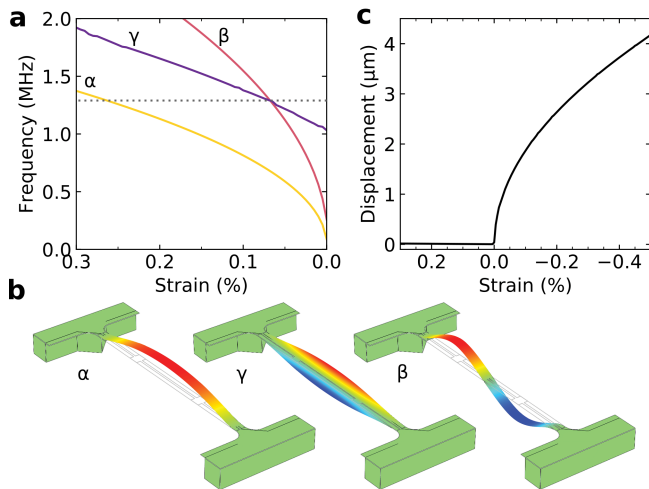


FIG. 4. **Finite element simulation of a strained WO_3 microbridge.** (a) Strain-dependence of the first flexural (α , β) and torsional (γ) mechanical modes and (b) corresponding mode shapes. (c) Vertical displacement of the microbridge center as a function of strain.

plane strain of our experimental device. As an additional reference point, we note that in the experimental data of Fig. 2(d) the frequency of mode α at $t = 0$ corresponds approximately to the frequency of the avoided mode crossing. Using this information in Figure 4(a), we can estimate the initial strain of the microbridge to be about $\varepsilon_0 = 0.25\%$ (grey dotted line). Surprisingly, this value is rather small compared to the epitaxial mismatch of 3.4% between WO_3 and the SrTiO_3 substrate. However, this can be explained considering that oxide compounds can easily accommodate stress with the formation of dislocations or point defects, such as oxygen vacancies. In particular, previous work shows that a low concentration of oxygen vacancies during the growth of WO_3 is sufficient to determine a relatively large lattice expansion, thus effectively relaxing the strain while maintaining a high crystal quality.[12]

It is possible to estimate the total experimental variation of the microbridge strain from the c -axis expansion Δc measured by XRD (Fig. 1). For this purpose, we note that by taking into account the different constraints for an epitaxial film and a freestanding structure we have

$$\frac{\Delta c}{c_0} = \left(\frac{1 + \nu}{1 - \nu} \right) \Delta \varepsilon, \quad (3)$$

with out-of-plane lattice parameter in the undoped state c_0 , Poisson ratio ν , and total strain variation $\Delta \varepsilon$ (see Supporting Information, Sec. IX). With the parameters employed in the simulation we obtain $\Delta \varepsilon = 0.75\%$. Taking the initial microbridge strain as +0.25% for the discussion above, we can estimate the strain in the saturated doping condition to be about -0.5% . On the basis of this analysis, we calculate the vertical displacement of the microbridge centre as a function of strain in Fig. 4(c). For positive (tensile) strain the displacement is negligible, while beyond the critical value ε_c

the structure relaxes the negative (compressive) strain by bending. At $\varepsilon = -0.5\%$ the simulation gives a displacement of $4 \mu\text{m}$, a value compatible with the optical measurements of Fig. 3. We note that the crossing point between tensile and compressive strain ($\varepsilon_c \sim 0$) lies at one third of the estimated range of experimental strain in Fig. 4(c). This is in good agreement with the experimental data of Fig. 2(d), where the critical condition of region (ii) lies also at about one third of both the total time and the electrical conductivity spans. Finally, we emphasize that in MEMS/NEMS devices it is particularly difficult to generate large compressive stress, a condition that usually requires additional components such as electrostatic actuators, piezoelectric elements or resistive heaters. These components present important drawbacks such as difficulty of focusing the actuation force on the resonator beam, hurdles in high-purity material fabrication, and insurgence of high temperatures. Our approach involving chemical doping proved to be a fundamental step forward over the present difficulties, providing a pathway for strong and localized strain-control of micro and nanodevices.

CONCLUSION

In summary, we demonstrated a new effective approach for controlling in situ the stress state of oxide-based freestanding structures. We achieved reversible control of the mechanical properties of single-crystal WO_3 microbridges, where the large lattice expansion due to hydrogen intercalation allowed us to finely tune the stress state from tensile to compressive, with a final buckled configuration. The proposed approach could be extended in two directions. By exploring the mechanical response of other oxides micromechanical systems to hydrogen doping. By realizing full-oxide heterostructures comprising a WO_3 layer acting as functional strain-tuning element. Our work highlights the potential of complex oxides to realise tunable nanomechanical systems or novel sensing devices.

METHODS

Device fabrication: The single-crystal 50 nm-thick WO_3 thin film on TiO_2 -terminated $\text{SrTiO}_3(001)$ substrate was grown by pulsed laser deposition using 500 °C substrate temperature, 8×10^{-2} mbar oxygen pressure, 1 J cm^{-2} laser fluence, and 1 Hz repetition rate. Pt was deposited by e-beam evaporation, its growth rate was monitored using a quartz microbalance. The process was stopped at an equivalent thickness of 0.2 nm. The microbridge structures were realised by a two-step electron-beam patterning using PMMA resist. The first patterning step was used to define the geometry of high-reflectivity mirrors and low-impedance microwire, followed by electron-beam evaporation of a 5/45 nm Ti/Au

overlayer and lift-off in acetone. The second patterning step defined the microbridge mesa and was followed by a 6 min Ar etching process (10 mA beam current, 500 eV beam energy, and 7×10^{-4} mbar pure Ar atmosphere), during which a total of 60 nm of $\text{WO}_3/\text{SrTiO}_3$ heterostructure was removed. The microbridges are finally made freestanding by selectively etching the SrTiO_3 substrate in a 4% aqueous solution of HF at 30 °C for 30 min, resulting in a total of 7 μm vertical distance between the etched substrate and the freestanding WO_3 .

Measurement setup: The electrical conductance measurements were performed using a four-probe DC configuration on a patterned square of the clamped WO_3 film. Contacts to the WO_3 film were provided by wire-bonding Ti/Au metal pads. The mechanical measurements were performed in a custom setup featuring a controlled gas atmosphere, temperature stability of ± 50 mK, motion detection of microstructures with optical lever technique and electrical pass-through. The optical images of Fig. 3 were acquired with an Olympus microscope equipped with an UMPlan FI 100X/0.90 objective lens.

Mechanical measurements: The mechanical modes of the microbridges are excited by biasing the device with an AC voltage across the metal microwire of the form $V(t) = V_0(1 + \sin(\omega t))$. Two concurrent mechanisms determine the appearance of a mechanical force: magnetomotive and electro-thermal. The magnetomotive mechanism arises from the Lorentz force exerted on the current flowing in the microbridge by the magnetic field of a permanent magnet located in the sample chamber. The electrothermal mechanism is due to the periodic thermal expansion and contraction of the microbridge determined by periodic Joule heating. Since the resistance of the metal microwire ($\sim 50 \Omega$) much lower than the one of the WO_3 bridge, even in its most-doped state, the current flowing in the wire does not depend on WO_3 doping conditions, hence providing a constant excitation magnitude. We note that the film thickness of 50 nm was chosen to have resonance frequencies falling within the accessible measurement range of our detector (2 MHz) and homogenous doping in the out-of-plane direction. Thinner samples would improve both aspects, but with the risk of lowering the fabrication yield. The data in Fig. 2 were acquired using a HP4395a vector network analyser with a 1 kHz bandwidth and 5 averages taken over a period of 20 s. Details of the optical setup are reported in the Supporting Information, Sec. VI.

Finite element simulation: Finite element analysis was performed in Comsol Multiphysics® using the structural mechanic module. The calculations employed the “static” and “prestressed eigenfrequency” solvers with a parametric sweep of the strain value. The mechanical parameters used to model the WO_3 microbridge are $E = 300 \text{ GPa}$, $\nu = 0.25$ and $\rho = 7600 \text{ kg m}^{-3}$, while Au was modelled using the standard material library provided by the software. Further details and device geometry are discussed in the Supporting Information, Sec. VIII.

CONTRIBUTIONS

N.M. and G.M. designed the experiment and performed the mechanical measurements. N.M. designed the device geometry and performed the finite element analysis. G.M. fabricated the device and performed the XRD, SEM, and optical measurements. M.P. provided the structural analysis leading to Eq. (3). W.J.V. designed and realized the mechanical characterization setup. N.M. and G.M. wrote the manuscript, with inputs from all authors.

ACKNOWLEDGEMENT

We thank P. G. Steeneken, L. Pellegrino, and D. Marré for helpful discussions and valuable comments on the manuscript. This work was supported by The Netherlands Organisation for Scientific Research (NWO/OCW) as part of the Frontiers of Nanoscience program (NanoFront). This work was supported by the EU through the European Research Council Advanced grant No. 677458 (AlterMateria). We acknowledge received funding from the project Quantox of QuantERA ERA-NET Cofund in Quantum Technologies (Grant Agreement N. 731473) implemented within the EU H2020 Programme.

SUPPORTING INFORMATION

Growth and surface analysis of WO_3 thin film, structural analysis by X-ray diffraction, device fabrication, pictures of the final devices, mechanical properties of microbridges of different lengths, details of the finite element model, and analytic model of strain in clamped and free-standing thin films.

[1] Judith L. MacManus-Driscoll, Patrick Zerrer, Haiyan Wang, Hao Yang, Jongsik Yoon, Arnaud Fouchet, Rong Yu, Mark G Blamire, and Quanxi Jia, “Strain Control and Spontaneous Phase Ordering in Vertical Nanocom-

posite Heteroepitaxial Thin Films.” *Nat. Mater.* **7**, 314–320 (2008).

[2] James M. Rondinelli, Steven J. May, and John W. Freeland, “Control of Octahedral Connectivity in Perovskite

- Oxide Heterostructures: An Emerging Route to Multifunctional Materials Discovery," *MRS Bull.* **37**, 261–270 (2012).
- [3] Ramamoorthy Ramesh and Darrell G. Schlom, "Creating Emergent Phenomena in Oxide Superlattices," *Nat. Rev. Mater.* **2019**, 1 (2019).
- [4] Nicola Manca, Luca Pellegrino, and Daniele Marré, "Reversible Oxygen Vacancies Doping in (La_{0.7},Sr_{0.3})MnO Microbridges by Combined Self-Heating and Electromigration," *Appl. Phys. Lett.* **106**, 203502 (2015), arXiv:1702.00826.
- [5] Jessica G. Swallow, Jae Jin Kim, John M. Maloney, Di Chen, James F. Smith, Sean R. Bishop, Harry L. Tuller, and Krystyn J. Van Vliet, "Dynamic Chemical Expansion of Thin-Film non-Stoichiometric Oxides at Extreme Temperatures," *Nat. Mater.* **16**, 749–754 (2017).
- [6] Lide Yao, Sampo Inkinen, and Sebastiaan Van Dijken, "Direct Observation of Oxygen Vacancy-Driven Structural and Resistive Phase Transitions in La_{2/3}Sr_{1/3}MnO₃," *Nat. Commun.* **8**, 1–9 (2017).
- [7] Kelvin H. L. Zhang, Guoqiang Li, Steven R. Spurgeon, Le Wang, Pengfei Yan, Zhaoying Wang, Meng Gu, Tamas Varga, Mark E. Bowden, Zihua Zhu, Chongmin Wang, and Yingge Du, "Creation and Ordering of Oxygen Vacancies at WO₃- δ and Perovskite Interfaces," *ACS Appl. Mater. Interfaces* **10**, 17480–17486 (2018).
- [8] Çetin Kiliç and Alex Zunger, "n-Type Doping of Oxides by Hydrogen," *Appl. Phys. Lett.* **81**, 73–75 (2002).
- [9] Jiang Wei, Heng Ji, Wenhua Guo, Andriy H. Nevidomskyy, and Douglas Natelson, "Hydrogen Stabilization of Metallic Vanadium Dioxide in Single-Crystal Nanobeams," *Nat. Nanotechnol.* **7**, 357–362 (2012).
- [10] Hyojin Yoon, Minseok Choi, Tae-Won W Lim, Hyunah Kwon, Kyuwook Ihm, Jong Kyu Kim, Si-Young Y Choi, and Junwoo Son, "Reversible Phase Modulation and Hydrogen Storage in Multivalent VO₂ Epitaxial Thin Films," *Nat. Mater.* **15**, 1113–1119 (2016).
- [11] Hanen Hamdi, Ekhard K. H. Salje, Philippe Ghosez, and Eric Bousquet, "First-Principles Reinvestigation of Bulk WO₃," *Phys. Rev. B* **94**, 245124 (2016).
- [12] Giordano Mattoni, Alessio Filippetti, Nicola Manca, Pavlo Zubko, and Andrea D. Caviglia, "Charge Doping and Large Lattice Expansion in Oxygen-Deficient Heteroepitaxial WO₃," *Phys. Rev. Mater.* **2**, 053402 (2018), arXiv:1711.05106.
- [13] X Leng, J Pereiro, J. Strle, G. Dubuis, A. T. Bollinger, A. Gozar, J. Wu, N. Litombe, C. Panagopoulos, D. Pavuna, and I. Božović, "Insulator to Metal Transition in WO₃ Induced by Electrolyte Gating," *npj Quantum Mater.* **2**, 35 (2017).
- [14] Yingge Du, Meng Gu, Tamas Varga, Chongmin Wang, Mark E. Bowden, and Scott A. Chambers, "Strain Accommodation by Facile WO₆ Octahedral Distortion and Tilting during WO₃ Heteroepitaxy on SrTiO₃(001)," *ACS Appl. Mater. Interfaces* **6**, 14253–14258 (2014).
- [15] J. S.E.M. Svensson and C. G. Granqvist, "Modulated Transmittance and Reflectance in Crystalline Electrochromic WO₃ Films: Theoretical Limits," *Appl. Phys. Lett.* **45**, 828–830 (1984).
- [16] J. S E M Svensson and C. G. Granqvist, "Electrochromic Coatings for Smart Windows: Crystalline and Amorphous WO₃ Films," *Thin Solid Films* **126**, 31–36 (1985).
- [17] C G Granqvist, "Electrochromic Tungsten Oxide Films: Review of Progress 1993-1998," *Sol. Energy Mater. Sol. Cells* **60**, 201–262 (2000).
- [18] Giordano Mattoni, Bas de Jong, Nicola Manca, Massimo Tomellini, and Andrea D. Caviglia, "Single-Crystal Pt-Decorated WO₃ Ultrathin Films: A Platform for Sub-ppm Hydrogen Sensing at Room Temperature," *ACS Appl. Nano Mater.* **1**, 3446–3452 (2018).
- [19] WA Crichton, Pierre Bouvier, and Andrzej Grzechnik, "The First Bulk Synthesis of ReO₃-Type Tungsten Trioxide, WO₃, From Nanometric Precursors," *Mater. Res. Bull.* **38**, 289–296 (2003).
- [20] I. Dass, J. Q. Yan, and B. Goodenough, "Oxygen Stoichiometry, Ferromagnetism, and Transport Properties of La_{2-x}NiMnO_{6+ δ} ," *Phys. Rev. B - Condens. Matter Mater. Phys.* **68**, 64415 (2003).
- [21] Harrie A.C. Tilmans, Miko Elwenspoek, and Jan H.J. Fluitman, "Micro Resonant Force Gauges," *Sensors Actuators A Phys.* **30**, 35–53 (1992).
- [22] C. S. Kim and S. M. Dickinson, "The Flexural Vibration of Slightly Curved Slender Beams Subject to Axial End Displacement," *J. Sound Vib.* **104**, 170–175 (1986).
- [23] S. Bouwstra and B. Geijselaers, "On the Resonance Frequencies of Microbridges," *TRANSDUCERS '91 1991 Int. Conf. Solid-State Sensors Actuators. Dig. Tech. Pap.*, 538–542 (1991).
- [24] A H Nayfeh and W Kreider, "Investigation of Natural Frequencies and Mode Shapes of Buckled Beams," *AIAA J.* **33**, 1121–1126 (1995).
- [25] Walter Lacarbonara, Haider N. Arafat, and Ali H. Nayfeh, "Non-Linear Interactions in Imperfect Beams at Veering," *Int. J. Non. Linear. Mech.* **40**, 987–1003 (2005).
- [26] Xing Liu and Hui-qing Fan, "Electronic Structure, Elasticity, Debye Temperature and Anisotropy of Cubic WO₃ from First-Principles Calculation," *R. Soc. Open Sci.* **5**, 171921 (2018).

Supporting Information

—

Large tunability of strain in WO₃ single-crystal microresonators controlled by exposure to H₂ gas

Nicola Manca^{†,1,2,3,*} Giordano Mattoni^{†,1,4} Marco Pelassa,⁵ Warner
J. Venstra,^{1,6} Herre S. J. van der Zant,¹ and Andrea D. Caviglia¹

¹*Kavli Institute of Nanoscience, Delft University of Technology,
P.O. Box 5046, 2600 GA Delft, The Netherlands*

²*Dipartimento di Fisica, Università degli Studi di Genova, via Dodecaneso 33, Genova, Italy*

³*CNR-SPIN Institute for Superconductors,
Innovative Materials and Devices, Corso Perrone 24, Genova, Italy*

⁴*Department of Physics, Graduate School of Science,
Kyoto University, Kyoto 606-8502, Japan*

⁵*Dipartimento Architettura e Design, Università degli Studi di Genova,
Stradone S. Agostino 37, Genoa, Italy*

⁶*Quantified Air BV, Rijnsburgersingel 77, 2316 XX Leiden, The Netherlands*

(Dated: October 28, 2019)

* manca@fisica.unige.it;

† Authors contributed equally

This supplemental material contains the following:

- Section I: Growth and surface analysis of WO_3 thin film.
- Section II: Structural analysis by X-ray diffraction.
- Section III: Device fabrication.
- Section IV: Pictures of the final devices.
- Section V: Mechanical properties of microbridges for different length.
- Section VI: Details of the optical setup.
- Section VII: Hydrogen deintercalation in a WO_3 microbridge.
- Section VIII: Details of the finite element modelling.
- Section IX: Strain in clamped and free-standing thin films.

Supporting Information, Sec. I. Growth and surface analysis of WO₃ thin film

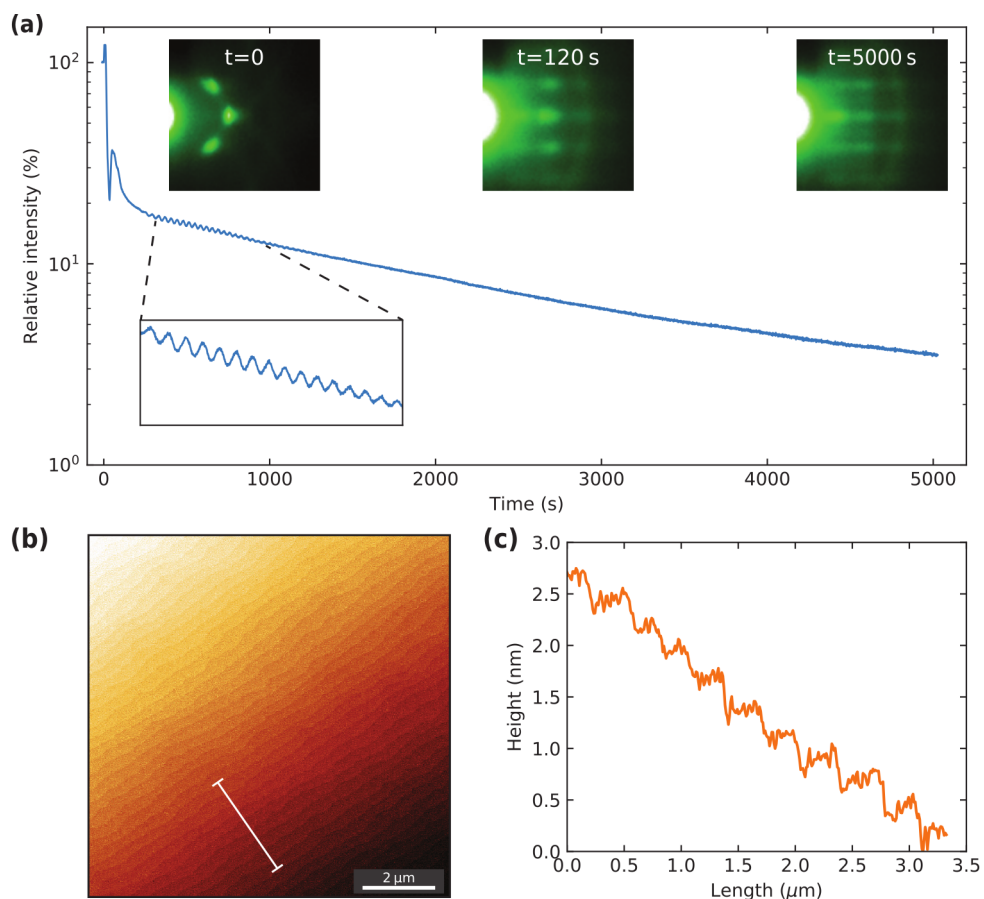


Figure S1. Surface analysis of the WO₃ thin films

Figure S1(a) shows the intensity over time of the RHEED (reflection high-energy electron diffraction) spot during the WO₃ growth. Intensity oscillations were employed to obtain a film with the desired thickness of about 50 nm, which was later confirmed by X-ray diffraction. The RHEED pattern before ($t = 0$ s), at the beginning ($t = 120$ s), and at the end of the deposition ($t = 5000$ s) is shown as insets. After the deposition, the sample surface was inspected by atomic force microscopy *ex situ*. Figure S1(b) shows the typical step-and-terrace structure of the SrTiO₃ substrate with single-unit-cell steps revealed by the line profile in Figure S1(c), indicating good crystal quality.

Supporting Information, Sec. II. Structural analysis by X-ray diffraction

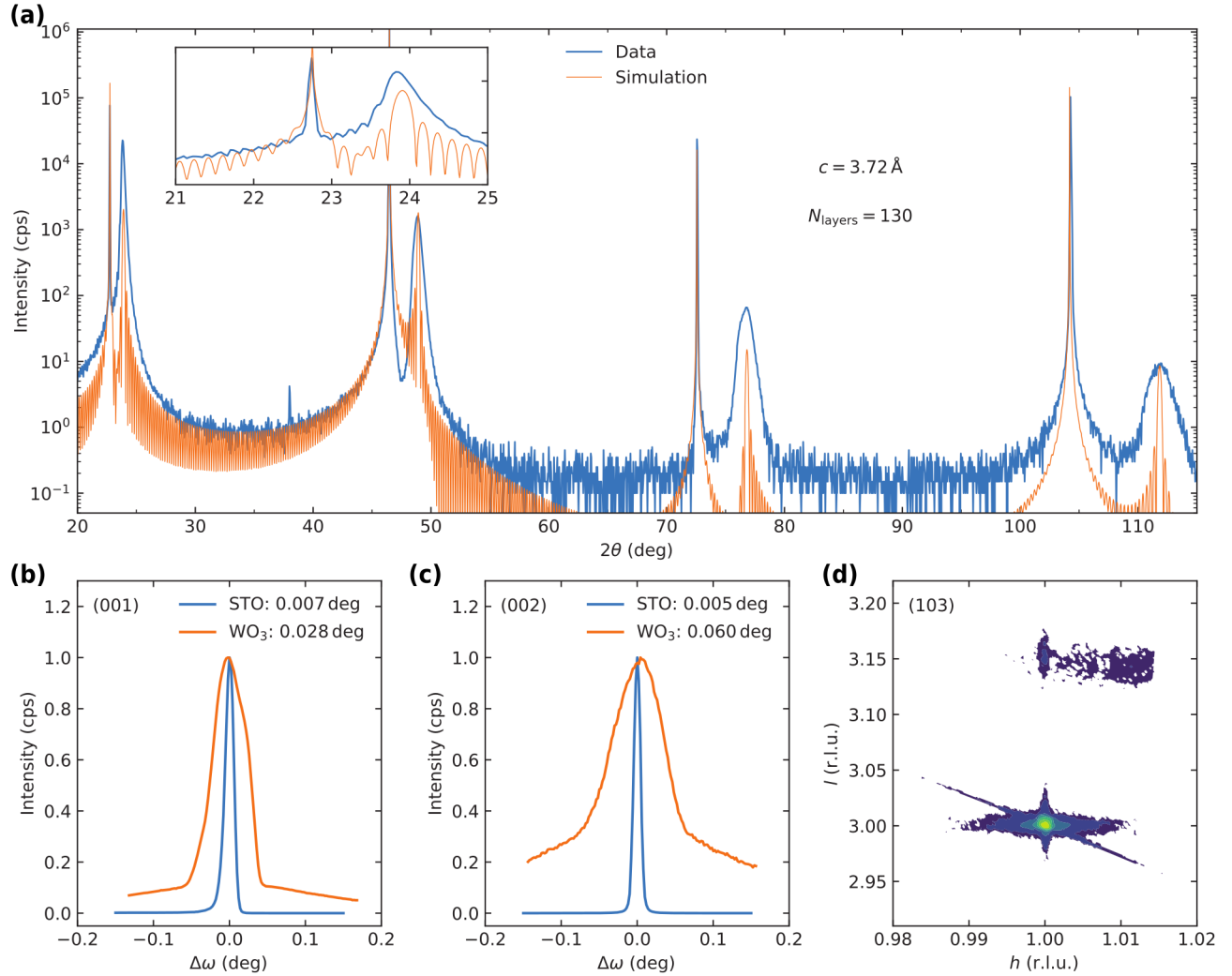


Figure S2. X-ray diffraction measurements of the WO_3 thin film on $\text{SrTiO}_3(001)$ substrate.

In Figure S2 we report a structural characterization of the WO_3 film by X-ray diffraction. Figure S2(a) is a $\theta - 2\theta$ scan showing the first four diffraction peaks of the SrTiO_3 substrate and WO_3 thin film. We compare the experimental measurement (blue line) with a simulated data (orange line) calculated with a classical kinematic scattering model with pseudocubic structure factor for the SrTiO_3 substrate and for an N -layer-thick WO_3 film. The atomic scattering factors are calculated using the data from http://wwwisis2.isis.rl.ac.uk/reference/Xray_scatterfac.htm. The model does not include strain relaxation and temperature effects. A magnification of the XRD data around the (001) peak is presented in the inset of Figure S2(a), where it is evident how the period

of the simulated finite size oscillations matches with the experimental data. Figure S2(b) and (e) show the rocking curves of the SrTiO₃ substrate and the WO₃ film around the (001) and (002) peaks, respectively, which have a remarkably low and comparable width. This indicates high coherence in the alignment of the lattice planes and it is a measure of single-crystal quality. The reciprocal space map in Figure S2(d) around the (103) diffraction peak of the substrate shows that the WO₃ peak is aligned along the same in-plane axis, indicating coherence between the substrate and film lattices.

Supporting Information, Sec. III. Device fabrication

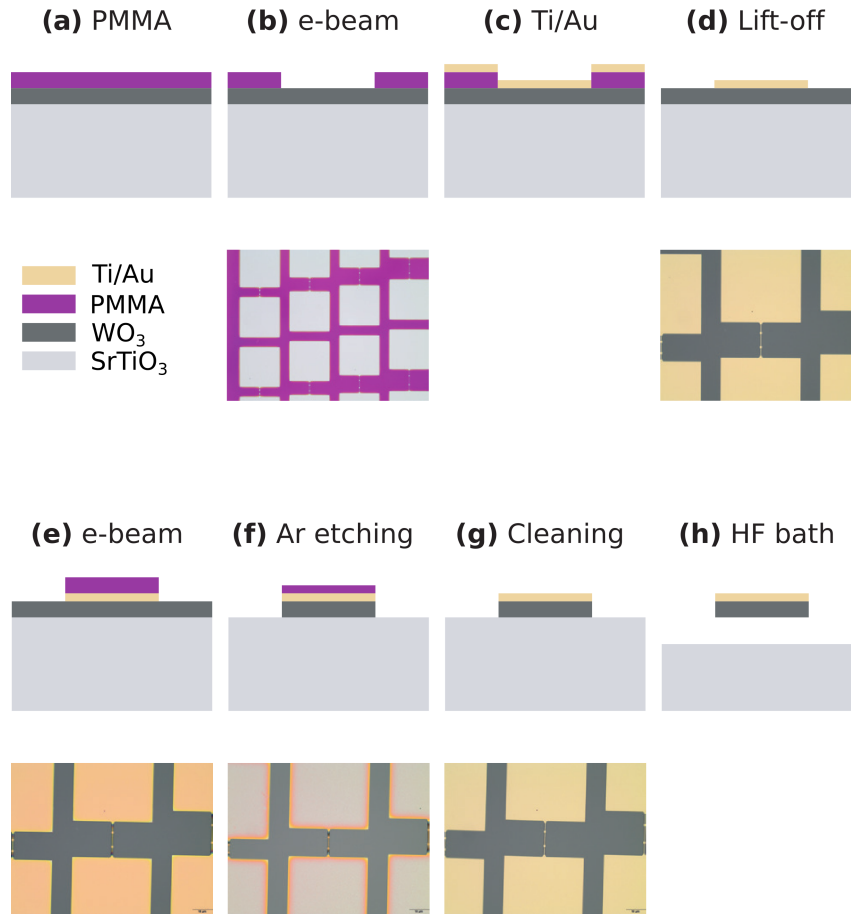


Figure S3. **Fabrication process of the WO₃ suspended microbridges.** Schematic drawing of the main fabrication steps discussed in this section (top) and corresponding optical images of the actual sample (bottom). The optical colors depend on the exposure conditions and differ across the pictures.

Figure S3 shows the main steps for the fabrication of the WO₃ suspended microbridges. Starting from a 50 nm single-crystal thin film of WO₃ grown on top of a SrTiO₃ (001) substrate, we first deposit 0.2 nm of Pt by thermal evaporation. This small amount does not realize a connected layer but provide Pt centres that catalyse the H₂ dissociation. Fabrication steps proceed as follows:

- (a) we deposit a layer of PMMA (A6-495) using a spin coater with revolution speed of 6000 rpm for about 50 s, which is baked at 180 °C for 10 min. Then, a thin layer of

Elektra 92 is deposited on top of the PMMA by spin coating, followed by a baking for 60 s at 100 °C.

- (b) the pattern for metallic regions is realized by electron beam (e-beam) lithography with a dose of 850 $\mu\text{C}/\text{cm}^2$.
- (c) a metal layer of 5 nm Ti and 45 nm Au is deposited by e-beam evaporation.
- (d) lift-off in warm acetone for 20 min at 60 °C.
- (e) a second e-beam step defines the microbridges pattern which is aligned with the metal layer.
- (f) to define the microbridge mesa we employed a dry etching technique (Ar milling, 500 eV, 0.2 mA/cm²).
- (g) a final cleaning was performed with NMP at 75 °C for 30min, followed by 10 min sonication in a ultrasound bath.
- (h) the structures are made suspended by soaking in an acid bath of HF (4 % in water) at 30 °C for 30 min with a magnetic stirrer spinning at 100 rpm. HF selectively etches the SrTiO₃ substrate without affecting the WO₃ film. Finally, the sample is dried using a critical point dryer.

Supporting Information, Sec. IV. Final devices

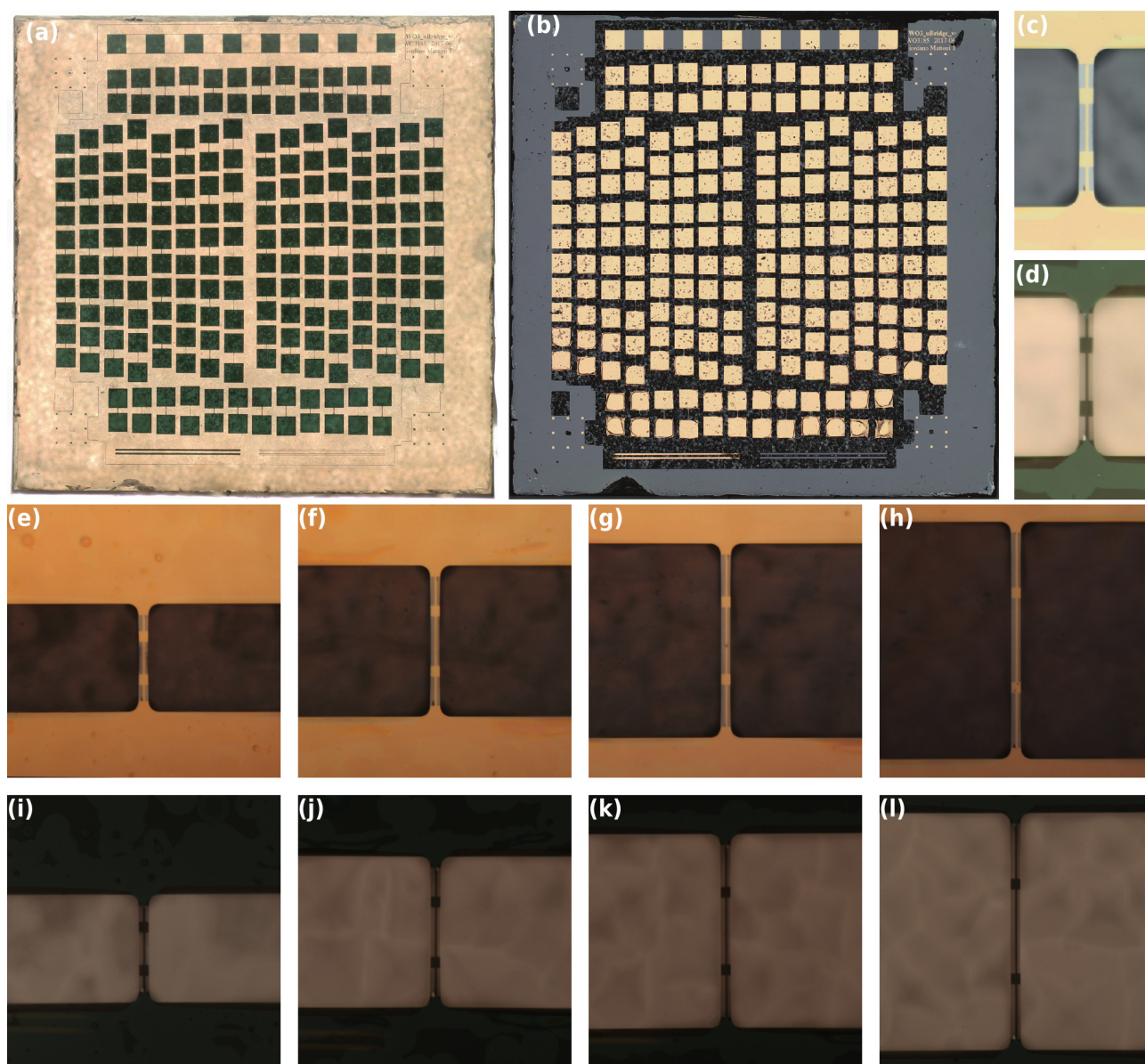


Figure S4. **Sample after the fabrication process** Pictures of the $5 \times 5 \text{ mm}^2$ sample in (a) transmitted and (b) reflected light. Pictures of a $50 \text{ }\mu\text{m}$ -long microbridge acquired in (c) reflected and (d) transmitted light. (e–l) Pictures of microbridges having different length ($50 \text{ }\mu\text{m}$, $70 \text{ }\mu\text{m}$, $90 \text{ }\mu\text{m}$, and $110 \text{ }\mu\text{m}$) acquired in reflected (top) and transmitted (bottom) light.

Supporting Information, Sec. V. Mechanical properties of microbridges for different length

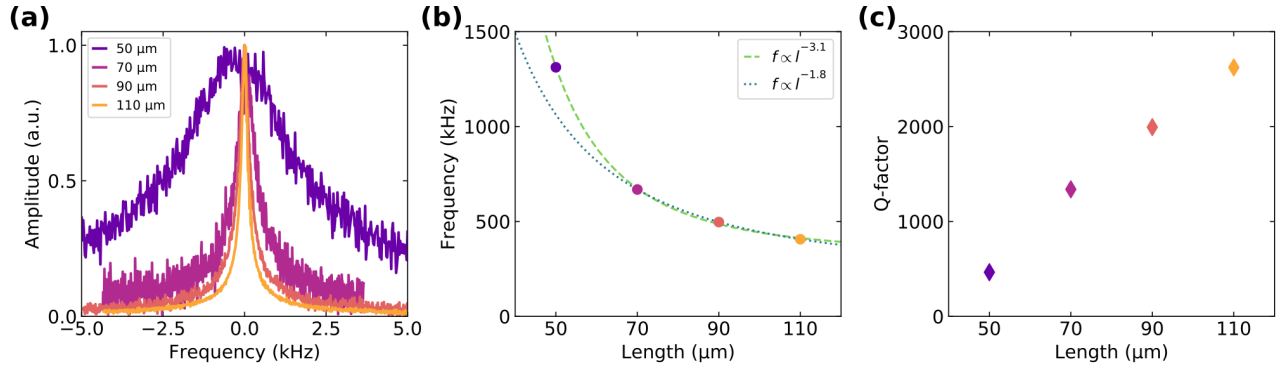


Figure S5. **First flexural mode for different bridge length** (a) Frequency response when driving beams of four different lengths near their fundamental flexural mode. The curves are normalized to the resonance frequency and the WO_3 material is in its pristine undoped state. (b) Extracted length dependence of the fundamental mode. The green dashed line is a fit with the power law $f \propto l^{-x}$ on the whole data range, while the blue dotted curve is a fit excluding the $l = 50 \mu\text{m}$ microbridge (blue dotted curve). (c) Extracted Q-factor for the different devices.

In Figure S5 we investigate the length dependence of the resonance frequency and quality factor of our microbridges. Eq. (1) reported in the main text has two limiting cases with respect to s , leading to the power law dependence

$$f_n \propto 1/l^p$$

where p equals 1 or 2 if s is dominant ('string' limit) or negligible ('beam' limit), respectively. By fitting the data in Fig. S5(b) we find $p = 3.1$ (green dashed line). This value lays outside the expected range, indicating a deviation from the ideal behavior. The deviation from the expected behaviour could be the result of the non-uniform geometry due to the localized mass of the gold mirrors, or losses due to the clamping region. Furthermore, the triangular undercut of the SrTiO_3 close to the clamping may be partially involved in the beam motion. Finally, an initial curvature may be present as a result of incorporated stress. The origin of the stress could be thermal mismatch during fabrication, stresses at the Au/WO_3 interface, and/or non-symmetric strain relaxation through the thickness of the WO_3 beam. We tentatively fit the experimental data by excluding the shortest ($l=50 \mu\text{m}$) bridge and find $p = 1.8$ (blue dotted line). The fact that this value lays inside

the expected range supports the idea that non-ideal boundary conditions, which are more relevant for shorter structures, are a critical parameter affecting the mechanical characteristics of our devices. This observation is corroborated by the trend of the corresponding Q-factor reported in Fig. S5(c), that increases from about 450 for $l = 50 \mu\text{m}$ up to 2600 for $l = 110 \mu\text{m}$. Longer structures are thus not only intrinsically more sensitive to stress variations, as shown by Eq. (1) in the main text, but also have lower mechanical dissipation and thus are more suitable to measure changes induced by H_2 gas.